Revision 2

Textural and compositional evolution of iron oxides at Mina Justa (Peru): implications for mushketovite and formation of IOCG deposits

Xia Hu[1,2,3,4], Huayong Chen[1,5*], Georges Beaudoin[3,4], Yu Zhang[6]

1. Key Laboratory of Mineralogy and Metallogeny, Guangzhou Institute of Geochemistry, Chinese Academy of Sciences, Guangzhou 510640, China

2. University of Chinese Academy of Sciences, Beijing 100049, China

3. Département de Géologie et de Génie Géologique, Université Laval, Québec, QC G1V 0A6, Canada

4. Research Center on the Geology and Engineering of Mineral Resources (E4m), Université Laval, Québec, QC G1V 0A6, Canada

5. Guangdong Provincial Key Laboratory of Mineral Physics and Materials, Guangzhou 510640, China

6. School of Geosciences and info-Physics, Central South University, Changsha 410083, China

[*] Corresponding author: huayongchen@gig.ac.cn

Address: Guangzhou Institute of Geochemistry, Chinese Academy of Sciences, P.O. Box 1131, Tianhe District, Guangzhou 510640, Guangdong PRC

ABSTRACT

Magnetite is a common mineral in many ore deposits and their host rocks. It contains a wide range of trace elements that can be used to fingerprint deposit type and hydrothermal processes. In this study, we present detailed textural and compositional data on magnetite of the Mina Justa deposit in southern Perú to constrain the formation of iron oxides in the Iron oxide Cu-Au (IOCG) deposit type.

Two types of magnetite, i.e., mushketovite (T_{M1}) and granular (T_{M2}) magnetite are identified based on their morphology. Mushketovite shows three different zones (central bright, dark and outer bright) in BSE (backscattered electron) images. The central bright part (T_{M1}-1), characterized by abundant porosity and inclusions, was intensively replaced by dark magnetite of the median rim (T_{M1}-2). The outer rim (T_{M1}-3) is also bright but lacks porosity and inclusions. Granular magnetite (T_{M2}) is anhedral and shows two different brightness (dark and bright) in BSE images. The dark (T_{M2}-1) and bright (T_{M2}-2) domains are intergrown, with irregular boundaries. In general, the dark zones of both magnetite types (T_{M1}-2 and T_{M2}-1) are characterized by higher Si, Ca, Al and lower Fe contents than the bright zones. Additionally, the lattice parameters of the two types of magnetite are similar and slightly lower than that of pure magnetite, indicating that some cations (e.g., Si^{4+}, Al^{3+}) whose ionic radii are smaller than Fe^{2+} or Fe^{3+} entered into the magnetite structure by simple or coupled substitutions.

Our study shows that oxygen fugacity and temperature change are the dominant mechanisms leading to the formation of different types of magnetite at Mina Justa.

Primary hematite, identified by Laser Raman analysis, was transformed into magnetite (T_{M1}-1) due to a sharp decline of fO_2 and then replaced by T_{M1}-2 magnetite during temperature increase, followed by formation of T_{M1}-3 due to decreasing temperature, eventually forming the mushketovite with different zones. The granular magnetite may have originally precipitated from hydrothermal fluid which crystallized T_{M2}-1 and also T_{M1}-2 magnetite, and was then modified by changing temperature and fO_2 to form T_{M2}-2. Even though the iron oxides in IOCG deposits may have formed in the same alteration stage, they could undergo a very complicate evolution process. Therefore, it is very important to combine texture and mineral chemistry to investigate the origin and evolution history of iron oxides.

Keywords: Iron oxides, mushketovite, texture, mineral chemistry, hydrothermal fluids, IOCG deposit

INTRODUCTION

Magnetite is a common mineral in many igneous, metamorphic and sedimentary rocks, as well as in various Fe-containing deposit-types, including Kiruna-type, BIF (banded iron formation), magmatic Fe-Ti oxide, Fe-skarn, IOCG and porphyry deposits (Williams et al., 2005; Liang et al., 2009; Groves et al., 2010; Sillitoe et al., 2010; Dupuis and Beaudoin, 2011; Huberty et al., 2012; Nadoll et al., 2012; Hu et al., 2015; Hu et al., 2017; Wen et al., 2017; Yin et al., 2017; Huang et al., 2018). Magnetite has an inverse spinel structure and typically incorporates a variety of minor and trace elements such as Mg, Al, Ti, V, Cr, Ni, Si, Ca, and Mn into its structure (Dupuis and Beaudoin, 2011; Dare et al., 2012; Nadoll et al, 2014). Previous studies have shown that compositional variety in magnetite can be used to fingerprint various deposit types or ore-forming processes (Carew 2004; Singoyi et al., 2006; Rusk et al., 2009; Dupuis and Beaudoin, 2011; Dare et al., 2012; Nadoll et al., 2012; Knipping et al., 2015). However, other studies (e.g., Hu et al., 2015; Wen et al., 2017; Yin et al., 2017) have also shown that the chemical composition of magnetite can be significantly modified or reequilibrated by hydrothermal fluid.

The iron oxide-copper-gold mineralization, characterized by Cu-sulfides±Au hydrothermal mineralization with abundant magnetite and/or hematite, has been a major exploration and research target since the discovery of the giant Olympic Dam Cu-U-Au (-REE) deposit (Hitzman et al., 1992). Magnetite and hematite from IOCG deposits have proven to be characterized by different trace elements, i.e., magnetite is characterized by higher Sn and Mn and lower V, Ti, Mg, Si, Cr, and Zn concentrations whereas hematite is characterized by higher As, Ga, Sb, and W concentrations (Carew, 2004). Huang et al. (2018) used trace element compositions of magnetite and hematite from 16 well-studied IOCG and IOA (iron oxide apatite) deposits to investigate the links between the chemical composition of iron oxides, hydrothermal processes and deposit subtypes. The above studies mainly focused on presenting geochemical data of iron oxides or using trace elements in iron oxides to constrain the formation of IOCG. However, it is equally important to investigate the textural evolution of iron oxides in IOCG deposits. In addition, magnetite in IOCG deposits commonly occurs as two different forms, i.e., mushketovite (a kind of platy magnetite which is formed by replacing specular hematite.) and granular magnetite (Marschik and Fontboté, 2001; Simard et al., 2006; Chen et al., 2010; Apukhtina et al., 2017). Previous studies commonly did not distinguish the two magnetite types and used their combined compositional data for deposit type discrimination (e.g. Zhibo and Chagangnuoer deposits, Günther et al., 2017). Most importantly, many researchers working in IOCG deposits usually immediately catalogue "platy magnetite" as mushketovite without detailed mineralogical studies (Chen et al., 2010; Apukhtina et al., 2017). However, some studies reported that platy magnetite may be originally magnetite which is crystallized from rapid cooling of fluid (Nystrom, 1994).

In this study, we use the Mina Justa deposit as an example to investigate magnetite mineralization in IOCG deposit. We present compositional data coupled with detailed texture anatomy of two textural types of magnetite. We provide powerful mineralogical evidence to support that platy magnetite in IOCG systems should be mushketovite. In addition, we discuss the factors controlling the magnetite chemistry and the links between the texture and chemical compositions of magnetite, to constrain the formation of iron oxides in the IOCG deposit based on these textural and geochemical analyses.

GEOLOGIC SETTING

The Mina Justa Cu deposit, with an indicated open pit resource of 346.6 Mt at an average grade of 0.71% Cu, 3.83 g/t Ag and 0.03 g/t Au (Chen et al., 2011), is located in the IOCG metallogenic belt in southern Peru (Fig. 1a). The deposit is hosted by the mid-late Jurassic Upper Río Grande Formation, which is dominated by plagioclase-phyric andesite and andesitic volcaniclastic units with minor sandstone, siltstone and limestone lenses (Fig. 1b; Caldas, 1978; Hawkes et al., 2002; Baxter et al., 2005).

Two primary areas of Cu orebodies have been delimited at Mina Justa, namely the main and upper orebodies, both of which are spatially associated with nearly parallel, NE-trending and shallowly SE-dipping faults, ranging from 10 m to 200 m in vertical extent (Fig. 1b; Chen et al., 2010; Baxter et al. 2005). The main mineralized body crops out as a 400 m long, discontinuous belt of Cu oxides with albite-K-feldspar-actinolite alteration (Fig. 1b), which dips 10° to 30° to the southeast. The similarly northeast-trending, but northwest-dipping magnetite lenses are also exposed on surface (Fig. 1b). They commonly contain minor Cu oxides and were locally cut by the southeast-dipping Mina Justa normal faults.

Four stages of hydrothermal alteration and mineralization were recognized at Mina Justa based on the detailed petrological studies: (I) an early alteration stage; (II) the hematite stage; (III) the magnetite-pyrite stage; and (IV) the Cu mineralization stage (Fig. 2, Chen et al., 2010). Stage I alteration mainly contains albite, microcline, diopside, and actinolite. The main stages associated with iron oxides at Mina Justa are stage II and stage III. Therefore, we will describe these two stages in details as follows. Stage II alteration is an obliterated hematite-dominant stage inferred from the existence of "mushketovite", magnetite unambiguously pseudomorphous after specular hematite (Chen et al., 2010). The hematite may have originally formed fractured plates. Anhedral-to-subhedral, and medium- to coarse-grained calcite is intergrown with the pseudomorphs, and was replaced by quartz and magnetite (Chen et al., 2010). This stage temporally separates the early alteration and the main magnetite alteration in andesite host. Stage III mainly contains magnetite, pyrite, quartz and chlorite. Pyrite is medium- to coarse grained and locally cut by chalcopyrite veins (Fig. 3a). Magnetite can be divided into two different types based on its morphology. One is mushketovite associated with pyrite and quartz (Fig. 3a). Chalcopyrite commonly occurs interstitially in mushketovite (Fig. 3a). The second is anhedral granular magnetite which has planar grain boundaries with pyrite and quartz (Fig. 3b). The Cu mineralization stage mainly contains Cu sulfides (e.g. chalcopyrite, bornite, chalcocite).

SAMPLING AND ANALYTICAL METHODS

Representative samples of two different types of magnetite from Stage III were selected for our study. All samples were prepared as standard polished thin sections and subsequently examined using the following analytical methods to determine the textural and compositional relationships.

Polished thin sections were carbon-coated and then investigated with a ΣIGMA scanning electron microscope (SEM) in BSE mode, at the School of Earth Science and Geological Engineering, Sun Yat-sen University (SYSU).

In situ micro-X-ray diffraction (XRD) experiments were conducted with a Rigaku D/max Rapis IIR micro-XRD system at the Central South University, Changsha, China. All measurements were carried out at 40 kV and 250 mA (CuKa) with a collection time of 22 min. The X-ray beam is ~40 μm in diameter and was focused on the selected spots on the thin sections. The software of MDI Jade 6.0 was used to analyze the obtained XRD patterns. We used this software to carry out whole pattern fitting refinement of the measured spectrum and then calculated lattice parameter. Because magnetite has a cubic structure, cell length “a” is the only parameter needed to be determined.

To identify whether hematite residue occurred in the platy magnetite, Raman spectra of magnetite were collected using a RM2000 laser micro-Raman spectrometer at the Key Laboratory of Mineralogy and Metallogeny of Guangzhou Institute of Geochemistry, Chinese Academy of Sciences (GIGCAS), Guangzhou, China. A 514.5 nm Ar laser was used and the laser spot is 2 μm in diameter. The scanning range was between 100 and 1500 cm^{-1}. The laser power reaching the sample surface was 10mW and the typical acquisition time was 60 s to avoid laser-induced thermal effects and oxidation.

The software of Adobe Photoshop CS4 was used to estimate the proportion of pore volume (approximately represented by area percentage) in the whole magnetite. The smallest unit of an image is a pixel and thus the area percentage can be represented by the pixel percentage. The pixels of pore area and whole magnetite area can be calculated by software, respectively. Therefore, the ratio of pixels in pore area and whole area is the proportion of pore volume in the whole magnetite.

The chemical composition of magnetite was analyzed using a JEOL JXA-8230 electron probe micro-analyzer (EPMA) at GIGCAS. The analyses were carried out with 15 kV voltage, 20 nA beam current and 1μm spot size. In addition, zoning in magnetite grains was mapped using EPMA for Fe, Si, Ca and Al. The operation conditions of an accelerate voltage of 20 kV, a probe current of 300 nA, a beam size of 1 to 4 μm and a dwell time of 100 to 200 ms for each point were used for mapping.

RESULTS

Morphology and texture of magnetite

Magnetite in the Mina Justa deposit can be classified into mushketovite (T_{M1}) and granular (T_{M2}) types. The T_{M1} magnetite commonly coexists with pyrite, quartz and chalcopyrite (Fig. 3a, b). It shows three different zones (central bright, median dark and outer bright rims) based on the SEM observation in BSE mode (Fig.4 b-d). The central bright part (T_{M1}-1 Mag) is characterized by abundant porosity and inclusions, and was replaced by the dark median rim (T_{M1}-2 Mag). Inclusions in T_{M1}-1 magnetite commonly consist of tiny W-bearing minerals such as scheelite (Fig.4d). The outer rim (T_{M1}-3 Mag) is also bright but lacks porosity and inclusions. The T_{M2} magnetite is usually intergrown with pyrite and quartz. It is commonly anhedral and shows two different brightness in BSE images. The dark (T_{M2}-1 Mag) and bright (T_{M2}-2 Mag) domains in this magnetite are intergrown with irregular boundaries (Fig.4f).

Structural characteristics of magnetite

XRD analysis results show that T_{M1} magnetite has cell parameter a = 8.3894 (0.00022) Å, which is slightly lower than that of pure magnetite (PDF No. 19-0629, a = 8.396 Å). The cell parameter (a) of the T_{M2} magnetite is 8.3909 (0.00019) Å, which is within error equal to that of T_{M1} magnetite. The full-width at half maximum (FWHM) of {311} peak of T_{M1} magnetite is 0.205°, and that of T_{M2} magnetite is 0.228° (Fig.5). Hence, T_{M1} magnetite may have higher crystallinity than T_{M2} magnetite (Crepaldi et al. 2003).

All samples exhibit Raman bands characteristic of magnetite (Wang et al., 2004), including a weak peak at ~298 and two stronger ones at ~540 and ~667 cm^{-1} (Fig. 6). The central bright zone (T_{M1}-1 mag, Fig. 4c,d) also exhibits Raman bands indicative of hematite at ca. 225, 406, and 1320 cm^{-1} (Giarola et al., 2012; Tan et al., 2015), implying that there are still hematite residue in the T_{M1}-1 magnetite (Fig.6).

Chemical composition of magnetite

The EMPA elemental mapping provided information on major and trace element distribution patterns within individual T_{M1} and T_{M2} magnetite crystals from the Mina Justa deposit (Fig. 7). Of the three main zones (one dark and two bright zones) in T_{M1} magnetite, the dark zone contains the highest contents of Si, Ca, Al but the lowest Fe content (Fig.7a). T_{M2} magnetite displays a similar variation trend as T_{M1} magnetite, in which the dark domain of magnetite is characterized by higher contents of Si, Ca, Al and lower Fe content than the bright domain (Fig.7b).

The average, minimum, and maximum chemical contents of the Mina Justa magnetite are presented in Table 1. Mushketovite forms three compositional groups, corresponding to three different zones (Fig.8). T_{M1}-1 magnetite has the lowest average SiO_2 (0.072 wt.%), Al_2O_3 (0.047 wt.%), MgO (0.016 wt.%) and the highest average total FeO (92.448 wt.%), whereas CaO is mostly below the detection limit (b.d.l). T_{M1}-2 magnetite has the highest average SiO_2 (1.582 wt.%), CaO (0.233 wt.%), Al_2O_3 (0.324 wt.%), MgO (0.12 wt.%) and the lowest average total FeO (90.28 wt.%). T_{M1}-3 magnetite contains moderately high average SiO_2 (0.505 wt.%), CaO (0.077 wt.%), Al_2O_3 (0.072 wt.%), MgO (0.036 wt.%) and moderately low average total FeO (91.938 wt.%). These three subtypes of magnetite contain similar MnO (0.047 wt.%, 0.064 wt.%, 0.039 wt.%, respectively), V_2O_3 (0.033 wt.%, 0.033 wt.%, 0.026 wt.%, respectively) and TiO_2 (0.012 wt.%, 0.031 wt.%, 0.014 wt.%, respectively) contents. The concentrations in NiO and Cr_2O_3 are mostly below the detection limit.

The granular magnetite forms two compositional groups, corresponding to two different zones (Fig.8). T_{M2}-1 magnetite has the higher average SiO_2 (1.365 wt.%), CaO (0.247 wt.%), Al_2O_3 (0.4 wt.%), MgO (0.221 wt.%), MnO (0.094 wt.%), TiO_2 (0.146 wt.%) and lower average total FeO (89.817 wt.%), V_2O_3 (0.256 wt.%). T_{M2}-2 magnetite is characterized by lower average SiO_2 (0.297 wt.%), Al_2O_3 (0.108 wt.%), MgO (0.041 wt.%), MnO (0.057 wt.%), TiO_2 (0.075 wt.%) and higher average total FeO (90.186 wt.%), V_2O_3 (0.424 wt.%). The contents of NiO, CaO and Cr_2O_3 are mostly below the detection limit. In general, the element contents (e.g., Si, Ca, Al) of the T_{M1}-2 and T_{M1}-3 magnetite are similar to those of the T_{M2}-1 and T_{M2}-2 magnetite, respectively. Whereas the concentration of V_2O_3 in T_{M1} is lower than T_{M2} magnetite (Fig.8).

DISCUSSION

Elemental substitution mechanisms in magnetite

Magnetite has an inverse spinel structure with a general formula XY_2O_4, where X represents a divalent cation such as Fe^{2+}, Mg, Mn, Ni, Co and Zn, and Y represents a trivalent or tetravalent cation such as Fe^{3+}, Al, V, Cr, Si and Ti (Wechsler et al., 1984; Nadoll et al., 2014). Tetrahedral sites in the magnetite structure are exclusively occupied by the ferric (Fe^{3+}) iron atoms, whereas octahedral sites are randomly occupied by ideally equal numbers of ferric (Fe^{3+}) and ferrous (Fe^{2+}) iron atoms (Lindsley, 1976; Wechsler et al., 1984; Nadoll et al., 2014). As reviewed by Nadoll et al. (2014), divalent cations such as Mg^{2+}, Mn^{2+}, Ca^{2+}, Zn^{2+}, and Ni^{2+} may enter into the magnetite structure by substituting Fe^{2+}, whereas Fe^{3+} can be replaced by some trivalent cations such as Al^{3+}, V^{3+} and Cr^{3+}. In addition, some tetravalent cations such as Ti^{4+}, Si^{4+} may enter into the magnetite structure when coupled with the substitution of a divalent cation (Wechsler et al., 1984; Newberry et al., 1982; Westendorp et al., 1991; Xu et al., 2014).

The lattice parameter of T_{M1} magnetite (8.389 Å) is subequal to that of T_{M2} magnetite (8.390 Å), which are somewht lower than that of the standard/pure magnetite (8.396 Å, Fukasawa et al., 1993). For magnetite at Mina Justa, the concentration of Fe^{3+} is negatively correlated with those of Si^{4+}, Fe^{2+}, Al^{3+} and Ca^{2+} (Fig. 9a, c, d, e) whereas the Fe^{2+} content is positively correlated with Si^{4+} (Fig. 9b), which may indicate that these elements were incorporated into the structural sites of magnetite by following substitution:

$$^{IV}Si^{4+} + {}^{VI}(Fe^{2+}, Ca^{2+}) \rightarrow {}^{IV}Fe^{3+} + {}^{VI}Fe^{3+} \qquad (1)$$

$$^{IV}Al^{3+} \rightarrow {}^{IV}Fe^{3+} \qquad (2)$$

In these substitutions, both Si^{4+} and $^{IV}Al^{3+}$ have smaller ionic radii than $^{IV}Fe^{3+}$ (Shannon, 1976), which may result in the lower lattice parameters of magnetite in Mina Justa compared to that of the standard magnetite. In addition, above correlations between those ions may be resulted from the presence of small inclusions of different minerals although they were not directly observed.

Genesis of mushketovite: transformation of hematite to magnetite

According to the Raman spectra (Fig. 6), T_{M1}-1 magnetite (central bright zone, Fig. 4c) exhibits characteristic Raman bands of residual hematite, which indicates that original hematite was transformed to magnetite. Such observation also provides convincing mineralogical evidence that platy magnetite should be mushketovite in previous studies at Mina Justa (Chen et al., 2010) and other IOCG deposits (such as Candelaria, Chile; Marschik and Fontboté, 2001).

There are two different transformation mechanisms of hematite to magnetite (Ohmoto, 2003; Mücke and Cabral, 2005). One is a redox reaction in which the Fe^{3+} ions in hematite are reduced to Fe^{2+} ions:

$$3Fe^{3+}{}_2O_3\ (Hem) + H_2 = 2Fe^{2+}\,Fe^{3+}{}_2\,O_4\ (Mag) + H_2O \qquad (3)$$

Another is a nonredox reaction in which the conversion of hematite to magnetite by a simple addition of Fe^{2+} ions：

$$Fe^{3+}{}_2O_3\ (Hem) + Fe^{2+} + H_2O = Fe^{2+}\,Fe^{3+}{}_2\,O_4\ (Mag) + 2H^+ \qquad (4)$$

In reaction (3), the amount of Fe atoms remains constant and there is only removal of oxygen. According to the cell volumes of magnetite (592.704 Å^3; Mücke and Cabral, 2005) and hematite (302.279 Å^3; Mücke and Cabral, 2005) and the amount of Fe atoms in them (24 in magnetite and 12 in hematite), it can be calculated that the replacement of hematite by magnetite causes a volume decrease of 1.64%. In contrast, in reaction (4), the amount of Fe atoms is not constant. The reaction has an iron ratio of 2:3 between the initial and the final products, which will cause an obvious increase in volume of 47.55%. According to Ohmoto (2003), this reaction may occur in many sedimentary iron formations. For magnetite from the Mina Justa deposit, the BSE images show that the central part of mushketovite (T_{M1}-1 Mag) contains abundant microporosity and inclusions (Fig. 4 c, d). The pore volume was estimated by the software of Adobe Photoshop CS4. As shown in Figure 10a, we mark out the pore area along its contour with Polygonal Lasso Tool of Adobe Photoshop CS4, i.e. white dashed circles, and attain the pixels of pore area and whole area, respectively (Fig. 10b, c). As a result, the ratio of pixels in pore area and whole area is the proportion of pore volume in the whole T_{M1}-1 magnetite grain, i.e. 1.61%, which is very close to the theoretic decreased volume (1.64%) in the reaction (3). This statement suggests that the abundant micropores in T_{M1}-1 magnetite resulted from the decrease in volume during transformation of hematite to magnetite, which means the reaction (3) may have occurred under a relative reduced environment.

Factors controlling magnetite composition

The composition of magnetite deposited from hydrothermal fluids is controlled by a number of factors, such as fluid composition, nature of co-crystallizing minerals, temperature (T) and oxygen fugacity (fO_2) during mineral formation (Nadoll et al., 2014). At Mina Justa, most magnetite precipitated during stage III, indicating that the two magnetite textures formed from similar hydrothermal fluids. The mushketovite and granular magnetite in Mina Justa deposit co-crystallized with the same assemblage, i.e., sulfides (pyrite and minor chalcopyrite) and quartz (with minor chlorite), suggesting the partitioning with co-crystallizing minerals had limited control on the composition of magnetite. Thus, the major controlling factors of distinct magnetite compositions at Mina Justa may be the temperature and oxygen fugacity.

Temperature is considered to be a major controlling factor for hydrothermal magnetite since element partition coefficients are temperature dependent (McIntire, 1963; Sievwright et al., 2017). High-temperature porphyry and skarn magnetite shows relatively high trace element contents, whereas un-metamorphosed magnetite from banded iron formation (BIF) has the lowest trace element contents (Nadoll et al., 2014). Titanium in Fe oxides is regarded to be positively correlated with temperature (Dare et al., 2012; Nadoll et al., 2012). In addition, according to Nadoll et al. (2014), to some extent, the Ti +V vs. Al+Mn plot can reflect the variation in temperature, with high temperature magnetite plotting at high Ti + V and Al + Mn values field. T_{M1}-2 magnetite has the highest Ti + V and Al + Mn contents (Fig.11a), indicating that temperature increased from T_{M1}-1 to T_{M1}-2, but then declined from T_{M1}-2 to T_{M1}-3 magnetite. T_{M2}-1 magnetite also has slightly higher Ti + V and Al + Mn contents than T_{M2}-2 magnetite, indicating that temperature declined from T_{M2}-1 to T_{M2}-2 magnetite. In general, T_{M2} may have formed in relatively higher temperatures than T_{M1}.

Oxygen fugacity can also impact the composition of magnetite by controlling element partition coefficients. Some elements, such as V, can occur in various valence states and therefore their behavior is strongly linked to fO_2 (Nielsen et al., 1994; Righter et al., 2006). The oxidation state of V in natural environments varies from +3 to +5. Among these species, V^{3+} has the highest compatibility with the spinel structure of magnetite (Balan et al., 2006; Righter et al., 2006). Vanadium is incompatible at high oxygen fugacity levels due to its 5+ oxidation state. Therefore, the partition coefficient of magnetite/liquid for V decreases with increasing fO_2 because V^{3+} is less stable under these conditions. For Mina Justa magnetite, the box and whisker plot of V (Fig. 11b) shows that the V contents of T_{M1} magnetite are lower than that of T_{M2} magnetite, indicating that the fO_2 of T_{M1} magnetite is higher than that of T_{M2} magnetite. This is consistent with mushketovite which is formed by replacing hematite. In addition, there are no significant variation of V contents in T_{M1}-1, T_{M1}-2 and T_{M1}-3 magnetite, suggesting that there was no significant changes in fO_2 among different zones of mushketovite (Fig. 11b). The T_{M2}-1 magnetite has slightly lower V content, indicating that fO_2 slightly decreased from the T_{M2}-1 to T_{M2}-2 magnetite.

Evolution process of iron oxides at Mina Justa

Based on above discussion, the primary hematite (Figure 12), which may have crystallized from an early-stage magmatic-hydrothermal fluid, was replaced by T_{M1}-1 magnetite after a sharply drop of fO_2 with abundant microporous and mineral inclusions due to shrinking of volume. Then T_{M1}-1 magnetite was replaced by hydrothermal fluids with increasing temperature that formed T_{M1}-2 magnetite with lower Fe and higher Si, Al, Ca concentrations. As the temperature decreased, less Si, Al, Ca entered into magnetite lattice to form T_{M1}-3 magnetite which lacks micropores and mineral inclusions. Hydrothermal fluids, likely the same that formed T_{M1}-2, directly precipitated granular magnetite (T_{M2}) with sulfides and quartz, supported by the higher temperature for T_{M2} compared to T_{M1} (Fig. 11a, 12). As the temperature decreased, together with a slight decrease in fO_2 (Fig. 11b), T_{M2}-2 magnetite precipitated with lower Si, Al, Ca and higher Fe and replaced T_{M2}-1 magnetite (Fig. 12).

IMPLICATIONS

This study provided mineralogical evidence to support that the platy magnetite in IOCG systems is mushketovite. In addition, textural and compositional data on magnetite from the Mina Justa deposit provide new insights into genetic mechanism of iron oxides in IOCG deposits. Oxygen fugacity and temperature changes are the dominant mechanisms leading to the formation of different types of magnetite. The primary hematite transformed into magnetite (T_{M1}-1) due to a decline in fO_2 and then replaced by T_{M1}-2 magnetite with increased temperature. Meanwhile, granular T_{M2}-1 magnetite directly precipitated from hydrothermal fluid. With the decrease of temperature, T_{M1}-2 and T_{M2}-1 magnetite are replaced by T_{M1}-3 and T_{M2}-2 magnetite, respectively. This study shows that even though the iron oxides may have formed from the same alteration stage in hydrothermal deposits, they could undergo a very complicated process of evolvement.

ACKNOWLEDGEMENTS

This study was funded by the National Natural Science Foundation of China (41572059 and U1603244) and the China Scholarship Council Fund (201804910485). We would like to thank prof. Xiangping Gu (Central South University) and Dr. Changming Xing (Guangzhou Institute of Geochemistry, Chinese Academy of Sciences) for their help in the XRD and EMPA analyses. Discussion with Xiaoliang Liang and Wei Tan (Guangzhou Institute of Geochemistry, Chinese Academy of Sciences) improved the understanding of the structure of magnetite and hematite. We also acknowledge constructive comments and suggestions from Irene del Real Contreras and an anonymous reviewer, and editorial handling by Melinda Dyar.

REFERENCES CITED

Apukhtina, O.B., Kamenetsky, V.S., Ehrig, K., Kamenetsky, M.B., Maas, R., Thompson, J., Mcphie, J., Ciobanu, C.L., Cook, N.J. (2017) Early, deep magnetite-fluorapatite mineralization at the Olympic Dam Cu-U-Au-Ag deposit, South Australia. Economic Geology, 112, 1531–1542.

Balan, E., De Villiers, J.P.R., Eeckhout, S.G., Glatzel, P., Toplis, M.J., Fritsch, E. (2006) The oxidation state of vanadium in titanomagnetite from layered basic intrusions. American Mineralogist, 91, 953–956.

Baxter, R., Meder, K., Cinits, R., Berezowski, M. (2005) The Marcona copper project—Mina Justa prospect geology and mineralisation. Proceedings of the 3rd Congr Int de Prospectores y Exploradores, Lima, Conferencias, Inst de Ingenieros de Minas del Perú, Lima (CD-ROM).

Caldas, V.J. (1978) Geología de los cuadrángulos de San Juan, Acarí y Yauca: hojas, (31-m, 31-n, 32-n). Instituto de Geología y Minería, Lima, Peru.

Carew, M.J. (2004) Controls on Cu-Au mineralization and Fe oxide metasomatism in the Eastern Fold Belt, N.W. Queensland, Australia. Ph.D thesis, James Cook University, Queensland.

Chen, H.Y., Clark, A.H., Kyser, T.K., Ullrich, T.D., Baxter, R., Chen, Y.M., Moody, T.C. (2010) Evolution of the Giant Marcona-Mina Justa Iron Oxide-Copper-Gold District, South-Central Peru. Economic Geology, 105, 155–185.

Chen, H., Kyser, T.K., Clark, A.H. (2011) Contrasting fluids and reservoirs in the contiguous Marcona and Mina Justa iron oxide–Cu (–Ag–Au) deposits, southcentral Perú. Mineralium Deposita, 46, 677–706.

Chen, W.T., Zhou, M.F., Gao, J.F., Hu, R. (2015) Geochemistry of magnetite from Proterozoic Fe–Cu deposits in the Kangdian metallogenic province, SW China. Mineralium Deposita, 50, 795–809.

Crepaldi, E.L., de A.A Soler-Illia, G.J., Grosso, D., and Sanchez, C. (2003) Nanocrystallised titania and zirconia mesoporous thin films exhibiting enhanced thermal stability. New Journal of Chemistry, 27, 9–13.

Dare, S.A.S., Barnes, S.-J., and Beaudoin, G. (2012) Variation in trace element content of magnetite crystallized from a fractionating sulfide liquid, Sudbury, Canada: Implications for provenance discrimination. Geochimica et Cosmochimica Acta, 88, 27–50.

Dupuis, C., and Beaudoin, G. (2011) Discriminant diagrams for iron oxide trace element fingerprinting of mineral deposit types. Mineralium Deposita, 46, 319–335.

Fukasawa, T., Iwatsuki, M., Furukawa, M. (1993) State analysis and relationship between lattice constants and compositions including minor elements of synthetic magnetite and maghemite. Analytica chimica acta, 281(2), 413-419.

Giarola, M., Mariotto, G., Ajo, D. (2012) Micro-Raman investigations on inclusions of unusual habit in a commercial tanzanite gemstone. Journal of Raman Spectroscopy, 43, 556–558.

Groves, D.I., Bierlein, F.P., Meinert, L.D., and Hitzman, M.W. (2010) Iron oxide copper-gold (IOCG) deposits through Earth history: Implications for origin, lithospheric setting, and distinction from other epigenetic iron oxide deposits: Economic Geology, 105, 641–654.

Günther, T., Klemd, R., Zhang, X., Horn, I., Weyer, S. (2017) In-situ trace element and Fe-isotope studies on magnetite of the volcanichosted Zhibo and Chagangnuoer iron ore deposits in the Western Tianshan, NW China. Chemical Geology, 453, 111–127

Hawkes, N., Clark, A., Moody, T. (2002) Marcona and Pampa de Pongo: giant Mesozoic Fe-(Cu, Au) deposits in the Peruvian coastal belt. Hydrothermal iron oxide copper-gold and related deposits: a global perspective. Porter Geoscience Consultancy Publishing, Adelaide, 2, 115–130.

Hitzman, M.W., Oreskes, N., Einaudi, M.T. (1992) Geological characteristics and tectonic setting of Proterozoic iron oxide (Cu ± U ± Au ± REE) deposits. Precambrian Research, 58, 241–287.

Hu, H., Lentz, D., Li, J.-W., McCarron, T., Zhao, X.-F., and Hall, D. (2015) Reequilibration processes in magnetite from iron skarn deposits. Economic Geology, 110, 1–8.

Hu, X., Chen, H.Y., Zhao, L.D., Han, J.S., Xia, X.P., 2017. Magnetite geochemistry of the Longqiao and Tieshan Fe-(Cu) deposits in the Middle-Lower Yangtze River Belt: Implications for deposit type and ore genesis. Ore Geology Reviews, 89, 823–835.

Huang, X.W., Boutroy, E., Makvandi, S., Beaudoin, G., Corriveau, L. (2018) Trace element composition of iron oxides from IOCG and IOA deposits: relationship to hydrothermal alteration and deposit subtypes. Mineralium Deposita. https://doi.org/10.1007/s00126-018-0825-1

Huberty, J.M., Konishi, H., Heck, P.R., Fournelle, J.H., Valley, J.W., and Xu, H. (2012) Silician magnetite from the Dales Gorge Member of the Brockman Iron Formation, Hamersley Group, Western Australia. American Mineralogist, 97, 26–37.

Knipping, J.L., Bilenker, L.D., Simon, A.C., Reich, M., Barra, F., Deditius, A.P., Wälle, M., Heinrich, C.A., Holtz, F., and Munizaga, R. (2015) Trace elements in magnetite from massive iron oxide-apatite deposits indicate a combined formation by igneous and magmatic-hydrothermal processes. Geochimica et Cosmochimica Acta, 171, 15–38.

Liang, H.Y., Sun, W., Su, W.C., Zartman, R.E. (2009) Porphyry copper-gold mineralization at Yulong, China, promoted by decreasing redox potential during magnetite alteration. Economic Geology, 104, 587–596.

Lindsley, D.H. (1976) The crystal chemistry and structure of oxide minerals as exemplified by the Fe–Ti oxides. In: Rumble III, D. (Ed.), Oxide Minerals. Rev. Mineral. Mineral. Soc. American Mineralogist, pp. L1–L60.

Marschik, R., Fontboté, L. (2001) The Candelaria-Punta del Cobre Iron Oxide Cu-Au(-Zn-Ag) Deposits, Chile. Economic Geology, 96, 1799–1826.

McIntire, W.L. (1963) Trace element partition coefficients—a review of theory and applications to geology. Geochimica et Cosmochimica Acta, 27, 1209–1264.

Mucke, A., Cabral, A.R. (2005) Redox and nonredox reactions of magnetite and hem atite in rocks .Chemie der Erde , 65, 271–278 .

Nadoll, P., Mauk, J.L., Hayes, T.S., Koenig, A.E., Box, S.E. (2012) Geochemistry of magnetite from hydrothermal ore deposits and host rocks of the Mesoproterozoic Belt Supergroup, United States. Economic Geology, 107, 1275–1292.

Nadoll, P., Angerer, T., Mauk, J.L., French, D., and Walshe, J. (2014). The chemistry of hydrothermal magnetite: A review. Ore Geology Reviews, 61, 1–32.

Newberry, N.G., Peacor, D.R., Essene, E.J., and Geissman, J.W. (1982) Silicon in magnetite: High resolution microanalysis of magnetite-ilmenite intergrowths. Contributions to Mineralogy and Petrology, 80, 334–340.

Nielsen, R.L., Forsythe, L.M., Gallahan, W.E., Fisk, M.R. (1994) Major- and trace-element magnetite–melt equilibria. Chemical Geology, 117, 167–191.

Nyström, J.O., and Henríquez, F., 1994, Magmatic features of iron ores of the Kiruna type in Chile and

Sweden; ore textures and magnetite geochemistry: Economic Geology, 89, 820–839.

Ohmoto, H. (2003) Nonredox transformations of magnetite–hematite in hydrothermal systems. Economic Geology, 98, 157–161.

Righter, K., Leeman, W.P., Hervig, R.L. (2006) Partitioning of Ni, Co and V between spinel-structured oxides and silicate melts: importance of spinel composition. Chemical Geology, 227, 1–25.

Rusk, B., Oliver, N., Brown, A., Lilly, R., Jungmann, D. (2009) Barren magnetite breccias in the Cloncurry region, Australia: comparisons to IOCG deposits. 656–658.

Shannon, R.D. (1976) Revised effective ionic radii and systematic study of inter atomic distances in halides and chalcogenides. Acta Crystallographica, A32, 751–767.

Sievwright, R.H., Wilkinson, J.J., O'Neill, H.S.C., Berry, A.J. (2017) Thermodynamic controls on element partitioning between titanomagnetite and andesitic-dacitic silicate melts. Contrib Mineral Petrol, 172:62.

Sillitoe, R.H., 2010, Porphyry copper systems: Economic Geology, 105, 3-41.

Simard, M., Beaudoin, G., Bernard, J., Hupe, A. (2006) Metallogeny of the Mont-de-l'Aigle IOCG deposit, Gaspe Peninsula, Quebec, Canada. Miner Deposita, 41, 607–636.

Singoyi, B., Danyushevsky, L, Davidson, G.J., Large, R., Zaw, K. (2006) Determination of trace elements in magnetites from hydrothermal deposits using the LA-ICP-MS technique. Abstracts of Oral and Poster Presentations from the SEG 2006 Conference Society of Economic Geologist, Keystone, USA, pp. 367–368.

Tan, W., Wang, C.Y., He, H.P., Xing, C., Liang, X.L., and Dong, H. (2015) Magnetite-rutile symplectite derived from ilmenite-hematite solid solution in the Xinjie Fe-Ti oxide-bearing, mafic-ultramafic layered intrusion (SW China). American Mineralogist, 100, 2348–2351.

Toplis, M.J., and Corgne, A. (2002) An experimental study of element partitioning between magnetite, clinopyroxene and iron-bearing silicate liquids with particular emphasis on vanadium. Contributions to Mineralogy and Petrology, 144, 22–37.

Wang, A., Kuebler, K.E., Jolliff, B.L., and Haskin, L.A. (2004) Raman spectroscopy of Fe-Ti-Cr-oxides, case study: Martian meteorite EETA79001. American Mineralogist, 89, 665–680.

Wechsler, B.A., Lindsley, D.H., Prewitt, C.T. (1984) Crystal structure and cation distribution in titanomagnetites (Fe3 − xTixO4). American Mineralogist, 69, 754–770.

Wen, G., Li, J.W., Hofstra, A.H., Koenig, A.E., Lowers, H.A., Adams, D. (2017) Hydrothermal reequilibratino of igneous magnetite in altered granitic plutons and its implications for magnetite classification schemes: Insights from the Handan-Xingtai iron district, North China Craton. Geochimica et Cosmochimica Acta. 213, 255–270.

Westendorp, R.W., Watkinson, D.H., and Jonasson, I.R. (1991) Silicon-bearing zoned magnetite crystals and the evolution of hydrothermal fluids at the Ansil Cu-Zn mine, Rouyn-Noranda, Quebec. Economic Geology, 86, 1110–1114.

Williams, P.J., Barton, M.D., Johnson, D.A., Fontbote, L., De Haller, A., Mark, G., Oliver, N.H.S., and Marschik, R. (2005) Iron oxide copper-gold deposits: Geology, space-time distribution and possible modes of origin: Economic Geology 100th Anniversary Volume, p. 371–405.

Xu, H., Shen, Z., and Konishi, H. (2014) Si-magnetite nano-precipitates in silician magnetite from banded iron formation: Z-contrast imaging and ab initio study. American Mineralogist, 99, 2196–2202.

Yin, S., Ma, C.Q., Robinson, P.T. (2017) Textures and high field strength elements in hydrothermal magnetite from a skarn system: Implications for coupled dissolution-reprecipitation reactions. American Mineralogist, 102, 1045–1056.

Figure captions

Fig.1. (**a**) The position of the Mina Justa deposit within the IOCG metallogenic belt of southern Perú. (**b**) Geological map of the Mina Justa deposit, hosted by the Middle Jurassic Upper Río Grande Formation (modified after Chen et al., 2011). Ab = albite, Act = actinolite, Kfs = K-feldspar.

Fig.2. Alteration and mineralization paragenesis of the Mina Justa deposit. (Modified after Chen et al., 2011).

Fig.3. Photomicrographs of magnetite from the Mina Justa deposit. (**a**) Mushketovite intergrown with pyrite and locally cut by chalcopyrite veins; (**b**) Granular magnetite is usually anhedral and has planar grain boundaries with pyrite.

Mineral abbreviations: *Mag*: magnetite, *Ccp*: chalcopyrite, *Py*: Pyrite, *Q*: quartz.

Fig.4. Photomicrographs (**a**, **e**) and BSE images (**b**, **c**, **d**, **f**) of the Mina Justa magnetite. (**a**) Mushketovite (T_{M1}) with interstitial chalcopyrite. (**b-d**) BSE images of mushketovite, which shows different zones. T_{M1}-1 magnetite is bright with abundant porosity and inclusions. T_{M1}-2 magnetite is dark and replacing T_{M1}-1 magnetite with sharp contact between them. T_{M1}-3 magnetite is also bright but lack of porosity and inclusions. (**e**) Granular magnetite (T_{M2}). (**f**) T_{M2}-1 magnetite is replaced by T_{M2}-2 magnetite.

Mineral abbreviations: *Mag*: magnetite, *Ccp*: chalcopyrite, *Sch*: scheelite.

Fig.5. In situ XRD patterns of magnetite from the Mina Justa deposit compared with standard

magnetite (19-0629). In addition to magnetite, the XRD pattern also shows the characteristic peaks of other minerals coexisting with magnetite, such as chalcopyrite (T_{M1}) and apatite (T_{M2}). The circles are 40 μm in diameter and represent the test area.

Fig.6. Raman spectra of different magnetite textures in the Mina Justa deposit. All samples displayed the characteristic peaks of magnetite, including a weak peak at ~298 cm^{-1} and two stronger at ~540 and ~667 cm^{-1}. But characteristic vibrations of hematite at ~225, ~406 and ~1320 cm^{-1} (Giarola et al., 2012) also observed in the central bright zone of platy magnetite, which indicates that it transformed from hematite and still contains hematite residue.

Fig.7. EMPA mapping of selected elements in different magnetite from the Mina Justa deposit. (**a**) Mushketovite; (**b**) Granular magneite. All color scales are in weight percent.

Fig.8. Multi-element variation diagram of the average trace element concentrations in magnetite from the Mina Justa deposit.

Fig.9. Binary plots of magnetite from the Mina Justa deposit indicating that trace elements entered into magnetite by substitution of divalent, trivalent and/or tetravalent cations for iron. (**a**) Si^{4+} vs. Fe^{3+}; (**b**) Si^{4+} vs. Fe^{2+}; (**c**) Fe^{2+} vs. Fe^{3+}; (**d**) Al^{3+} vs. Fe^{3+}; (**e**) Ca^{2+} vs. Fe^{3+}; (**f**) $Si^{4+}+Al^{3+}$ vs. $Fe^{2+}+Ca^{2+}$.

Fig.10. The estimation of pore volume (manipulate by the software of Adobe Photoshop CS4). The smallest unit of an image is a pixel and thus the area percentage can be represented by the pixel percentage. (**a**) T_{M1}-1 magnetite with abundant porosity and inclusions. White dashed circles are the pore identified by the Polygonal Lasso Tool of software. (**b-c**) The pixels of pore area and whole T_{M1}-1 magnetite area calculated by software, respectively. Therefore, the ratio of pixels in pore area and whole area, i.e. 1.61%, is the proportion of pore volume in the whole T_{M1}-1 magnetite.

Fig.11. (a) Plot of (Al+Mn) vs. (Ti+V) for Mina Justa magnetite. The high temperature magnetite usually plotted into the high Ti + V and Al + Mn values field (Nadoll et al., 2014). (b) Plot of V concentration for Mina Justa magnetite. V^{3+} has the highest compatibility with the spinel structure of magnetite and V^{5+} is incompatible at high oxygen fugacity levels (Balan et al., 2006; Righter et al., 2006). Therefore, higher V concentration may indicate lower fO_2.

Fig.12. Schematic evolution-textural and chemical of iron oxides from the Mina Justa deposit. (a1-a4) primary hematite was replaced by T_{M1}-1 magnetite with the decrease of fO_2. Then T_{M1}-1 magnetite was replaced by hydrothermal fluids with increasing temperature that formed T_{M1}-2 magnetite. Finally, T_{M1}-3 magnetite was formed on the outside of T_{M1}-2 magnetite with the decrease of temperature. (b1-b2) Granular magnetite (T_{M2}-1) directly precipitated from hydrothermal fluids and then replaced by T_{M2}-2 magnetite with the decrease of temperature and fO_2.

Fig. 1

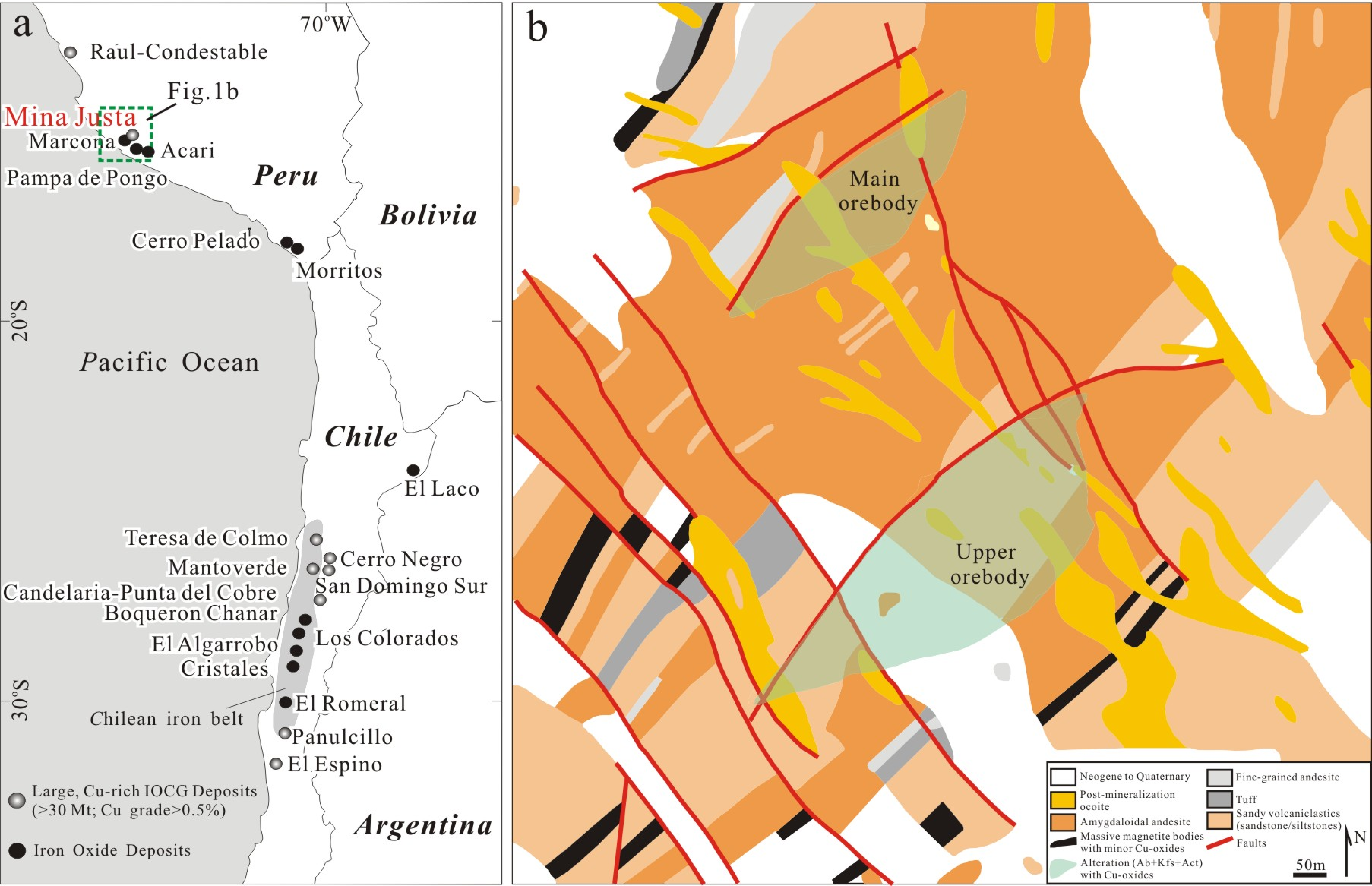
a
70°W
Raul-Condestable
Fig.1b
Mina Justa
Marcona
Acari
Pampa de Pongo
Peru
Bolivia
Cerro Pelado
Morritos
20°S
Pacific Ocean
Chile
El Laco
Teresa de Colmo
Mantoverde
Cerro Negro
San Domingo Sur
Candelaria-Punta del Cobre
Boqueron Chanar
Los Colorados
El Algarrobo
Cristales
El Romeral
30°S
Chilean iron belt
Panulcillo
El Espino
Large, Cu-rich IOCG Deposits (>30 Mt; Cu grade>0.5%)
Iron Oxide Deposits
Argentina
b
Main orebody
Upper orebody
Neogene to Quaternary
Post-mineralization ocoite
Amygdaloidal andesite
Massive magnetite bodies with minor Cu-oxides
Alteration (Ab+Kfs+Act) with Cu-oxides
Fine-grained andesite
Tuff
Sandy volcaniclastics (sandstone/siltstones)
Faults
N
50m

Fig. 2

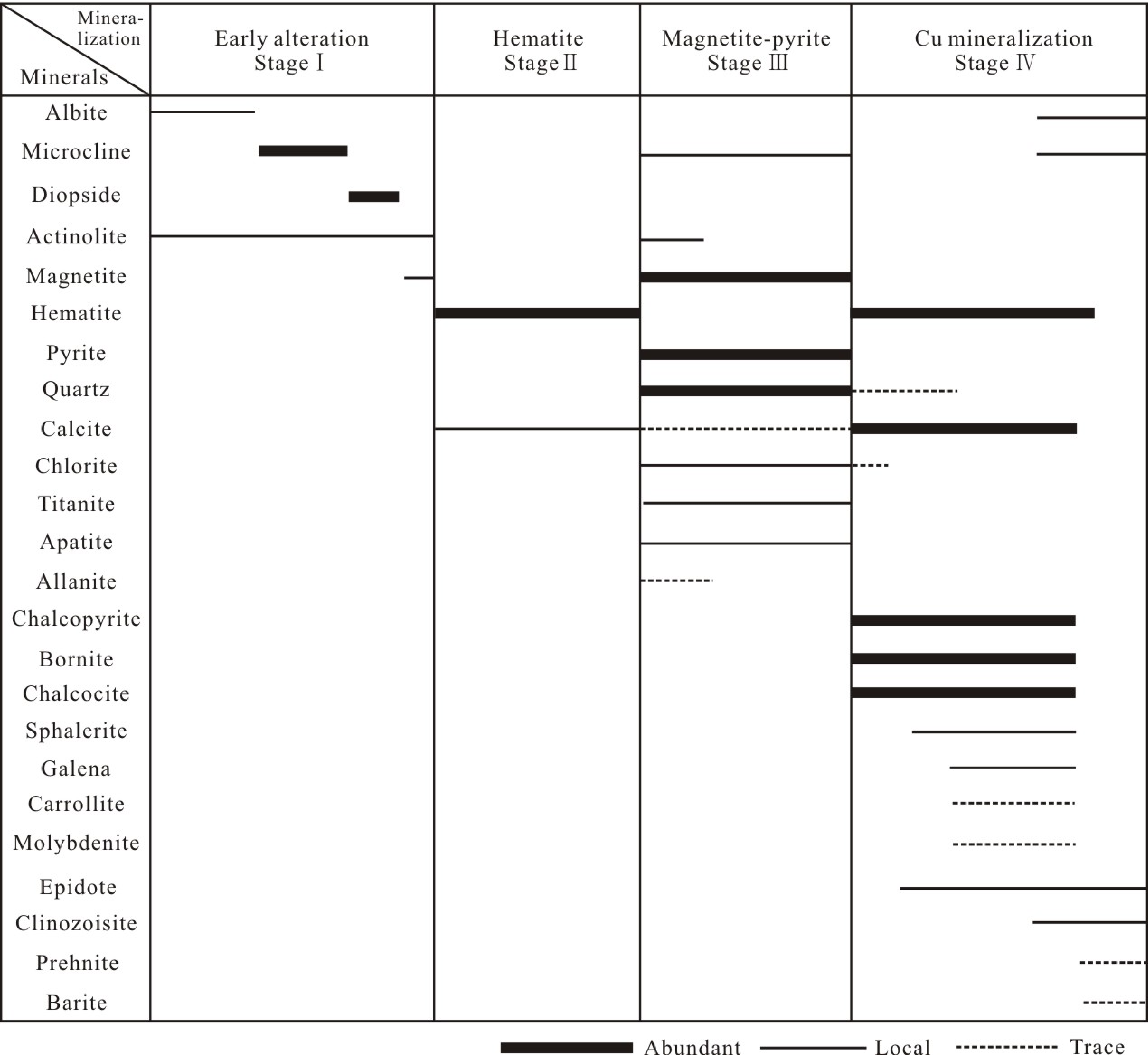
Mineralization
Minerals
Early alteration Stage Ⅰ
Hematite Stage Ⅱ
Magnetite-pyrite Stage Ⅲ
Cu mineralization Stage Ⅳ
Albite
Microcline
Diopside
Actinolite
Magnetite
Hematite
Pyrite
Quartz
Calcite
Chlorite
Titanite
Apatite
Allanite
Chalcopyrite
Bornite
Chalcocite
Sphalerite
Galena
Carrollite
Molybdenite
Epidote
Clinozoisite
Prehnite
Barite
Abundant
Local
Trace

Fig. 3

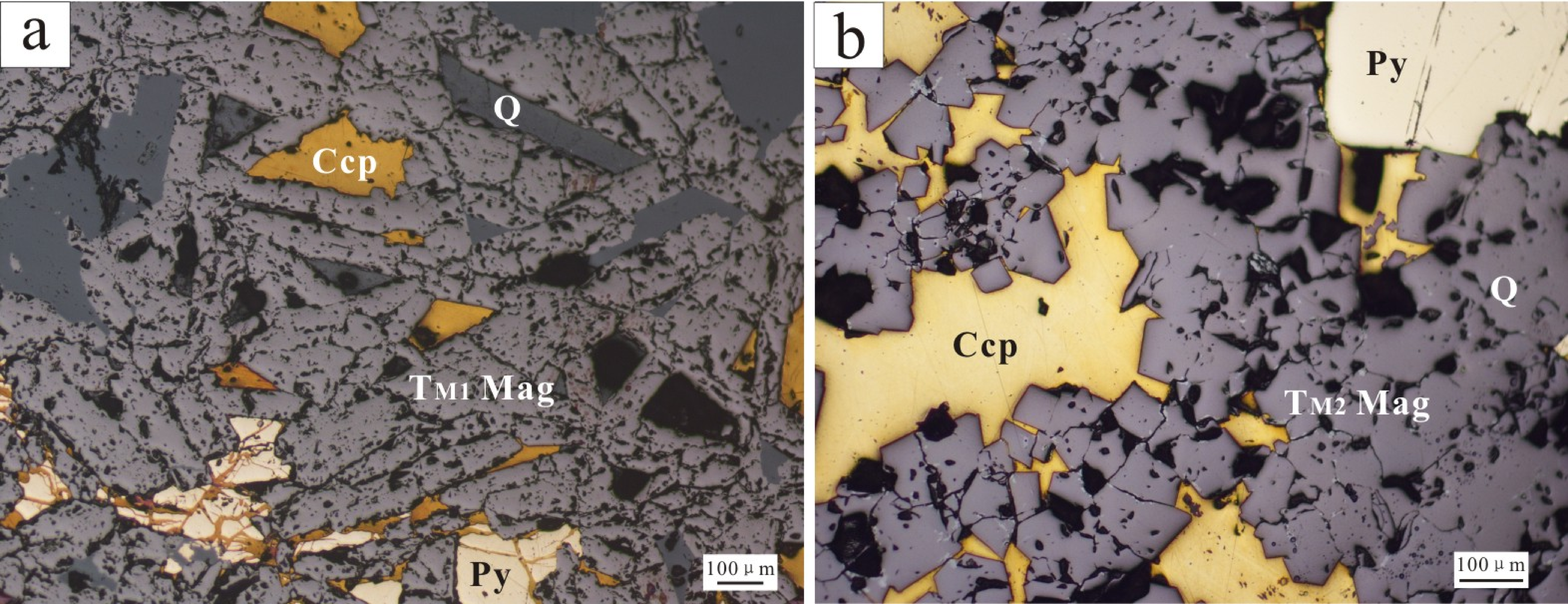

Fig. 4

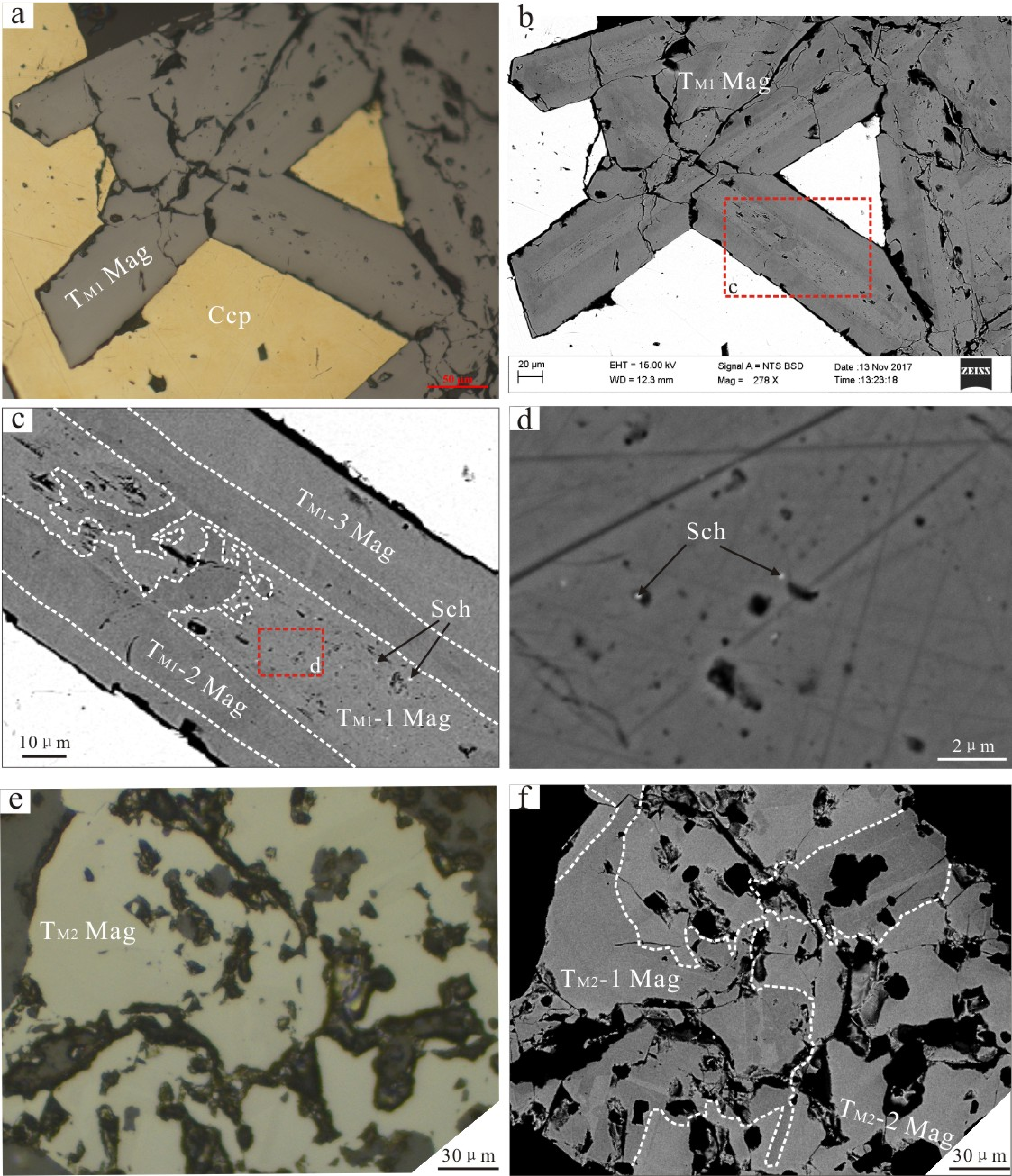
a
TM1 Mag
Ccp
50 µm
b
TM1 Mag
c
20 µm
EHT = 15.00 kV
WD = 12.3 mm
Signal A = NTS BSD
Mag = 278 X
Date :13 Nov 2017
Time :13:23:18
ZEISS
c
TM1-3 Mag
Sch
d
TM1-2 Mag
TM1-1 Mag
10 µm
d
Sch
2 µm
e
TM2 Mag
30 µm
f
TM2-1 Mag
TM2-2 Mag
30 µm

Fig. 5

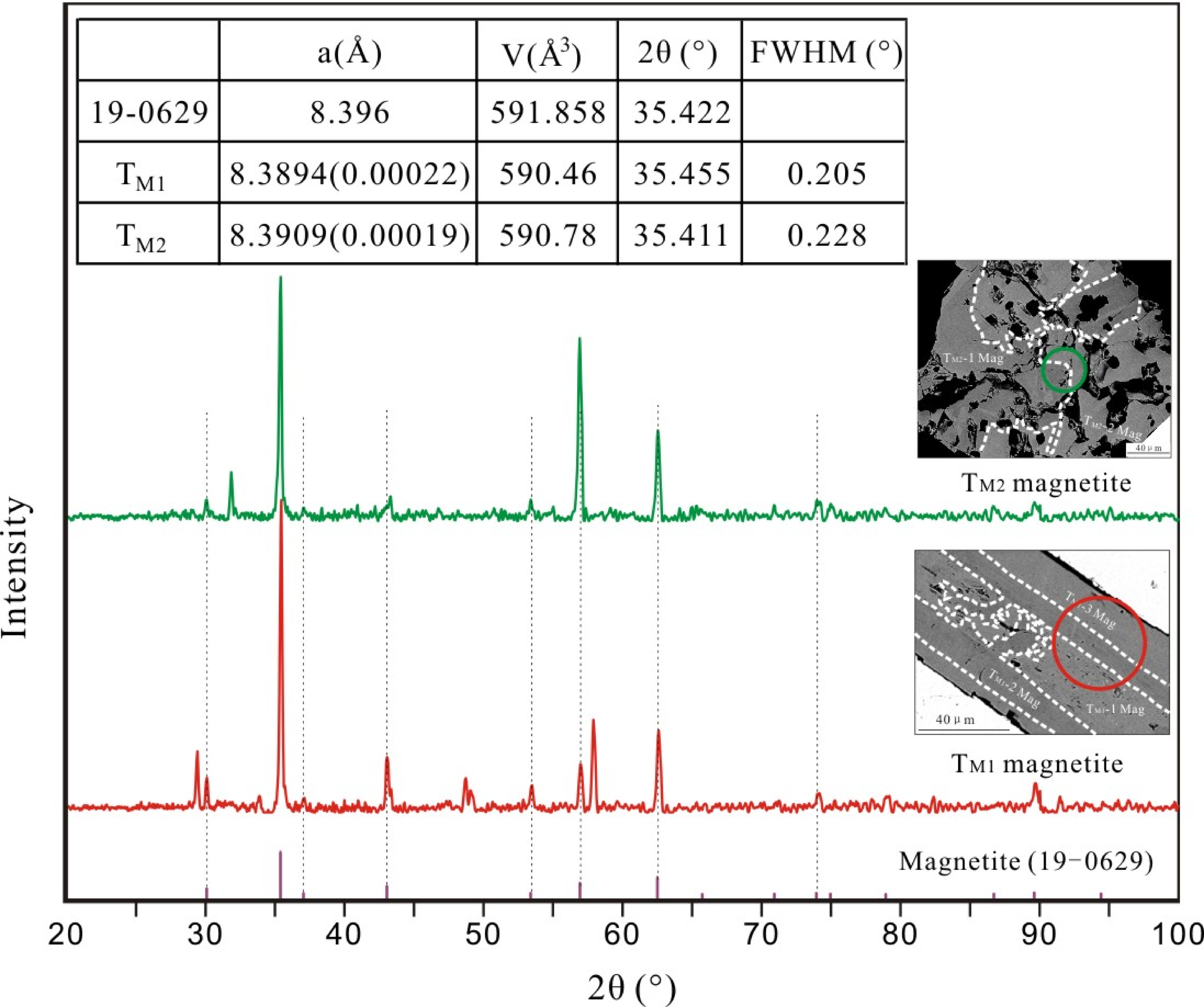

	a(Å)	V(Å^3)	2θ (°)	FWHM (°)
19-0629	8.396	591.858	35.422	
T_{M1}	8.3894(0.00022)	590.46	35.455	0.205
T_{M2}	8.3909(0.00019)	590.78	35.411	0.228

Fig. 6

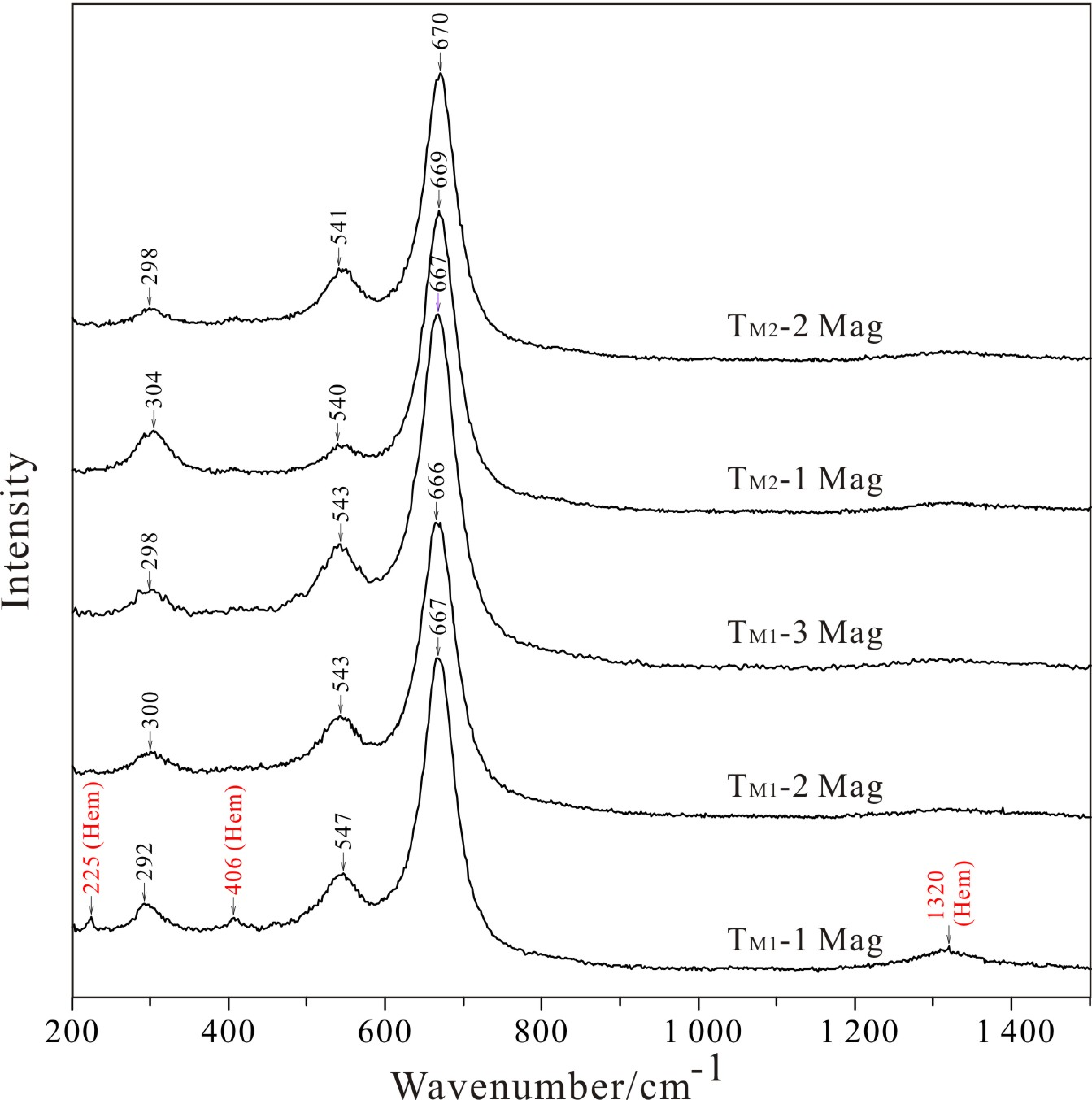
670
669
541
298
TM2-2 Mag
667
304
540
TM2-1 Mag
666
543
298
TM1-3 Mag
667
543
300
TM1-2 Mag
225 (Hem)
292
406 (Hem)
547
1320 (Hem)
TM1-1 Mag
Intensity
200
400
600
800
1 000
1 200
1 400
Wavenumber/cm-1

Fig. 7


(a)
(b)
TM1-2 Mag
TM1-1 Mag
TM1-3 Mag
Sch
20 μm
TM2-1 Mag
TM2-2 Mag
30 μm
Fe
wt.%
92
87
82
77
72
67
62
57
52
47
42
37
32
27
20 μm
Fe
wt.%
94
88
82
76
70
64
58
52
46
40
34
28
22
16
50 μm
Si
4.5
4.2
3.9
3.6
3.3
3
2.7
2.4
2.1
1.8
1.5
1.2
0.9
0.6
0.3
Si
4.5
4.2
3.9
3.6
3.3
3
2.7
2.4
2.1
1.8
1.5
1.2
0.9
0.6
0.3
Ca
0.75
0.7
0.65
0.6
0.55
0.5
0.45
0.4
0.35
0.3
0.25
0.2
0.15
0.1
0.05
Ca
1.35
1.26
1.17
1.08
0.99
0.9
0.81
0.72
0.63
0.54
0.45
0.36
0.27
0.18
0.09
Al
0.6
0.56
0.52
0.48
0.44
0.4
0.36
0.32
0.28
0.24
0.2
0.16
0.12
0.08
0.04
Al
3.75
3.5
3.25
3
2.75
2.5
2.25
2
1.75
1.5
1.25
1
0.75
0.5
0.25

Fig. 8

T_{M1}-1
T_{M1}-2
T_{M1}-3
T_{M2}-1
T_{M2}-2
T_{M1}-2
T_{M2}-1
T_{M1}-3
T_{M2}-2
T_{M1}-1
concentration (wt.%)
1
0.9
0.8
0.7
0.6
0.5
0.4
0.3
0.2
0.1
0
-0.1
Si
Ca
Ni
Mg
Al
Mn
Cr
V
Ti

Fig. 9

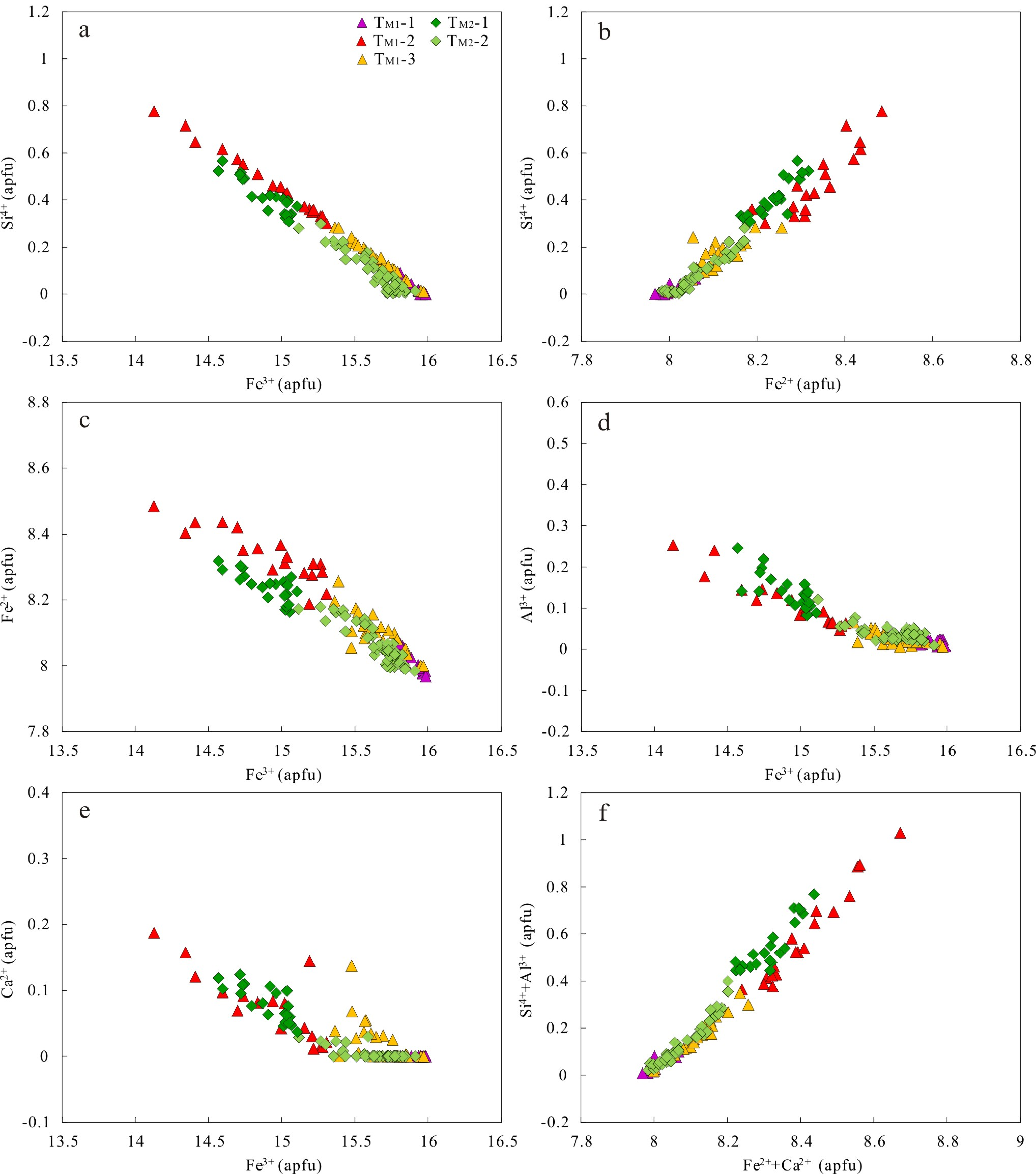
a
TM1-1
TM1-2
TM1-3
TM2-1
TM2-2
Si4+ (apfu)
1.2
1
0.8
0.6
0.4
0.2
0
-0.2
13.5
14
14.5
15
15.5
16
16.5
Fe3+ (apfu)
b
Si4+ (apfu)
7.8
8
8.2
8.4
8.6
8.8
Fe2+ (apfu)
c
Fe2+ (apfu)
8.8
8.6
8.4
8.2
8
7.8
Fe3+ (apfu)
d
Al3+ (apfu)
0.6
0.5
0.4
0.3
0.2
0.1
0
-0.1
-0.2
Fe3+ (apfu)
e
Ca2+ (apfu)
0.4
0.3
0.2
0.1
0
-0.1
Fe3+ (apfu)
f
Si4++Al3+ (apfu)
1.2
1
0.8
0.6
0.4
0.2
0
-0.2
7.8
8
8.2
8.4
8.6
8.8
9
Fe2++Ca2+ (apfu)

Fig. 10

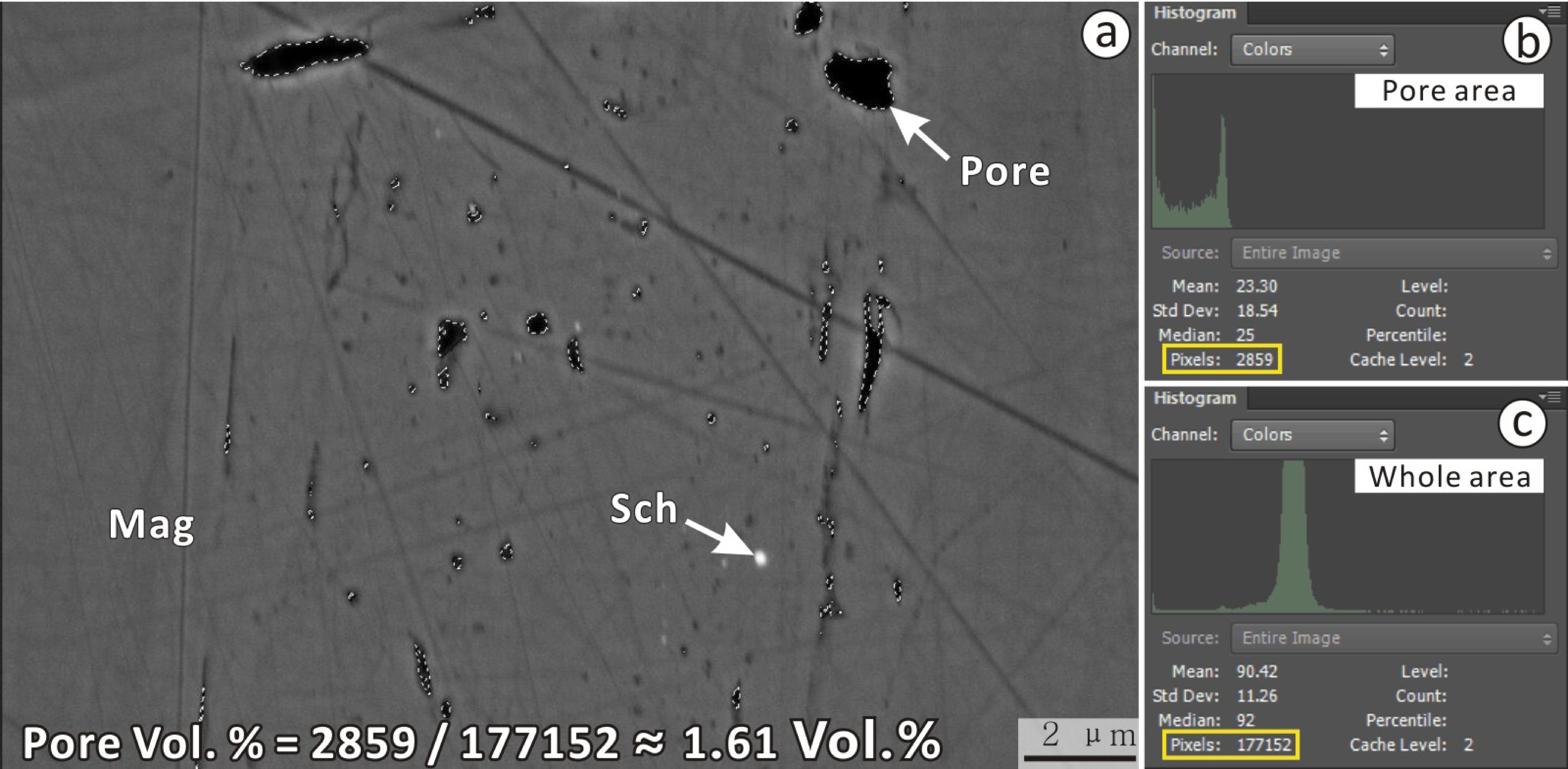

Pore Vol. % = 2859 / 177152 ≈ 1.61 Vol.%

Channel: Colors

Source: Entire Image

Mean: 23.30
Std Dev: 18.54
Median: 25
Pixels: 2859
Level:
Count:
Percentile:
Cache Level: 2

Channel: Colors

Source: Entire Image

Mean: 90.42
Std Dev: 11.26
Median: 92
Pixels: 177152
Level:
Count:
Percentile:
Cache Level: 2

Fig. 11


a
TM1-1
TM1-2
TM1-3
TM2-1
TM2-2
Decreasing temperature
Al+Mn (wt.%)
Ti+V (wt.%)
10
1
0.1
0.01
0.001
0.001
0.01
0.1
1
10
b
Mean
Median
V (ppm)
100000
10000
1000
100
10
1
0.1
TM1-1
TM1-2
TM1-3
TM2-1
TM2-2

Fig. 12


(a1)
Hem ?
Decreasing fO2
(a2)
Sch
TM1-1 Mag
(Porous with numerous mineral inclusions; Higher Fe and lower Si, Al, Ca)
Increasing temperature
(a3)
TM1- 1 Mag
Sch
TM1-2 Mag
(Lower Fe and higher Si, Al, Ca)
Decreasing temperature
(a4)
TM1- 1 Mag
TM1- 2 Mag
Sch
TM1- 3 Mag
(Lack of Porous and mineral inclusions; Higher Fe and lower Si, Al, Ca)
Replacement
Lower temperature
Higher fO2
Hydrothermal fluid
Precipitation
Lower fO2
Higher temperature
TM2-1 Mag
(Lower Fe, V; higher Si, Al, Ca)
(b1)
Decreasing temperature and fO2
(Higher Fe, V and lower Si, Al, Ca)
TM2-2Mag
TM2-1 Mag
(b2)

Table 1 Mean, minimum and maximum contents of electron microprobe analyses (wt.%) for magnetite from the Mina Justa deposit.

Magnetite type		SiO_2	CaO	NiO	MgO	FeO	Al_2O_3	MnO	Cr_2O_3	V_2O_3	TiO_2
T_{M1}-1 (n=13)	Mean	0.072	b.d.l	0.011	0.016	92.448	0.047	0.047	0.009	0.033	0.012
	Min	0.010	b.d.l	b.d.l	0.010	91.964	0.020	0.019	b.d.l	b.d.l	b.d.l
	Max	0.294	b.d.l	0.045	0.102	93.294	0.100	0.089	0.054	0.079	0.048
T_{M1}-2 (n=18)	Mean	1.582	0.233	0.005	0.120	90.280	0.324	0.064	0.011	0.033	0.031
	Min	0.984	0.035	b.d.l	0.010	88.834	0.132	0.014	b.d.l	b.d.l	b.d.l
	Max	2.612	0.588	0.026	0.321	92.266	0.723	0.106	0.030	0.085	0.106
T_{M1}-3 (n=22)	Mean	0.505	0.077	0.009	0.036	91.938	0.072	0.039	0.017	0.026	0.014
	Min	0.036	0.010	b.d.l	0.010	90.072	0.016	b.d.l	b.d.l	b.d.l	b.d.l
	Max	0.940	0.420	0.035	0.086	94.291	0.184	0.079	0.065	0.083	0.075
T_{M2}-1 (n=21)	Mean	1.365	0.247	0.004	0.221	89.817	0.400	0.094	0.013	0.256	0.146
	Min	1.031	0.115	b.d.l	0.082	87.324	0.233	0.022	b.d.l	0.046	0.075
	Max	1.898	0.383	0.045	0.437	91.236	0.690	0.155	0.060	0.561	0.237
T_{M2}-2 (n=45)	Mean	0.297	0.011	0.008	0.041	90.186	0.108	0.057	0.015	0.424	0.075
	Min	0.013	b.d.l	b.d.l	0.01	88.259	0.025	0.015	b.d.l	0.102	0.01
	Max	0.99	0.092	0.022	0.229	94.426	0.338	0.148	0.085	0.786	0.193

Abbreviation: n = numbers of analyses; b.d.l = below detection limits.